

Optimum choice of parameters and numerical schemes for a regional gravimetric Moho recovery



Samurdhika Rathnayake, Robert Tenzer*

Department of Land Surveying and Geo-Informatics, Hong Kong Polytechnic University, Hong Kong

ARTICLE INFO

Article history:

Received 28 March 2019

Accepted 20 May 2019

Available online 9 July 2019

Keywords:

Crust

Gravity

Moho inversion

Isostasy

ABSTRACT

Despite practical limitations of isostatic theories to model the Moho geometry are well-known, gravimetric methods are often used in terrestrial studies of crustal structure in regions with a low seismic data coverage. Moreover, these methods are indispensable in planetary studies. Various gravimetric methods have been proposed. The Airy and Pratt theories are defined based on adopting a local compensation mechanism. The Vening Meinesz theory assumes a regional isostatic flexural model. The Vening Meinesz regional isostatic model generally describes a response of the lithosphere to a load more realistically than the Airy model over continents. The Pratt method, on the other hand, better describes a compensation mechanism of the oceanic lithosphere. The application of a particular isostatic model also depends on applied numerical procedures, parameters for inversion, input data specifications, and many other aspects. In this study, we address some basic aspects by applying local and regional isostatic models for a Moho recovery. We also conduct a spectral analysis to assess a spectral resolution of gravity data that is optimal for a Moho recovery. Furthermore, we inspect the influence of low-degree spherical harmonics of gravity field on a Moho geometry. Gravimetric results are validated using seismic data at the European plate. Our results confirm a better performance of a regional compensation principle. We also demonstrate that a different thickness of the oceanic and continental crustal thickness should be taken into account as a priori information. Spectral analysis indicates that gravity data used for a Moho inversion should optimally have a spatial resolution between degrees 60 to 180. Results also show that low-degree spherical harmonics do not modify significantly the Moho geometry, particularly over regions with a relatively homogenous structure of deep mantle.

© 2019 Institute of Seismology, China Earthquake Administration, etc. Production and hosting by Elsevier B.V. on behalf of KeAi Communications Co., Ltd. This is an open access article under the CC BY-NC-ND license (<http://creativecommons.org/licenses/by-nc-nd/4.0/>).

1. Introduction

Various methods for a gravimetric Moho recovery have been developed and applied in global and regional studies. Gravimetric methods are typically formulated based on adopting some

hypothesis about the isostatic mass balance. The Pratt-Hayford model [1–3] assumes a variable density of compensation. The Airy-Heiskanen theory [4,5] is based on adopting a variable depth of compensation. Both these isostatic models are based on a local compensation mechanism. Vening Meinesz [6] modified the Airy theory by introducing a regional compensation scheme for a thin plate lithospheric flexure model. Parker [7] presented a practical iterative gravimetric method similar to the Vening Meinesz hypothesis. Oldenburg [8] added a filter in the frequency domain to stabilize the solution. The combination of these two methods was generalized to a 3D problem by Gomez-Ortiz and Agarwal [9] and applied, for instance, by Shin et al. [10] and Kiamehr and Gomes-Ortiz [11]. Moritz [12] generalized the Vening Meinesz inverse problem for a global compensation mechanism and adopted a spherical approximation of the Earth. A regional compensation model was later utilized also in the Parker-Oldenburg method [8] by assuming a variable crustal thickness and adopting a uniform

* Corresponding author. The Department of Land Surveying and Geo-Informatics, The Hong Kong Polytechnic University, 181 Chatham Road South, Kowloon, Hong Kong.

E-mail address: robert.tenzer@polyu.edu.hk (R. Tenzer).

Peer review under responsibility of Institute of Seismology, China Earthquake Administration.



Moho density contrast. Note that both, the Parker-Oldenburg and Moritz models use an interface detection theory [13]. It implies that the Bouguer gravity anomaly relates to elevation/depth at a certain position. The Parker-Oldenburg method was also presented for a planar approximation and solved by applying the Fast Fourier Transform (FFT) technique. Sjöberg [14] reformulated Moritz problem, called the Vening Meinesz-Moritz inverse problem of isostasy, as that of solving a non-linear Fredholm integral equation of the first kind. The solutions by Moritz [12] and Sjöberg [14] use the same idea, but the former (and also the Parker-Oldenburg method) applies an iterative approach while the latter provides a direct solution. Eshagh et al. [15] generalized the VMM isostatic model for a variable density distribution. Ye et al. [16] derived generalized expressions for solving the VMM problem in the spectral domain from gravity and gravity-gradient data and applied these spectral expressions for a global Moho recovery. Their results indicated that in global applications, using global data-coverage, the spherical harmonic expressions for the gravimetric forward and inverse modeling yield (almost) the same results for both, the input gravity and gravity gradient data.

One of the most important aspects of gravimetric methods for a Moho recovery is to apply the topographic and crust-stripping gravity corrections in order to reveal a Moho signature in gravity data. Various methods have been developed and applied for this purpose (e.g. [17–24]). Alternatively, spectral filtering methods could be used to remove a short-wavelength gravitational contribution of detailed topographic features and shallow anomalous crustal density structures as well as the long-wavelength signature of deep mantle density heterogeneities [14]. However, to know exactly which wavelengths should be filtered out, or which range of wavelengths should be used is not simple. Among several aspects to be taken into consideration, the most importance are the gravity-signal dependence on the target depth, spectrum analysis of the gravity field and other geophysical and geological information [25–27]. In this study, we model and remove gravitational contributions of anomalous crustal density structures based on available information from results of seismic surveys. We further take into account the upper mantle density distribution by assuming the variable Moho density contrast. To deal with the gravitational signature of deep mantle density heterogeneities, Bagherbandi and Sjöberg [28] removed the long-wavelength gravitational signal according to method proposed by Eckhardt [29]. He evaluated a maximum degree of long-wavelength spherical harmonics, which should be subtracted from the gravity field before solving the isostatic inverse problem. A theory of this method was based on finding a representative depth of the gravitational signal attributed to each spherical harmonic-degree term. The spherical harmonics which have the depth below a certain limit (chosen, for instance, as the maximum Moho depth) are then removed from the gravity field. Here we apply this approach to treat the long-wavelength mantle signal. Bagherbandi et al. [30] used an alternative approach by applying a non-isostatic correction.

In this study, we apply local and regional isostatic models to estimate a regional Moho geometry at the European plate and compare gravimetric results with existing seismic models. A detailed coverage by a high quality seismic data in this study area allows us to inspect some basic numerical aspects, particularly how the spectral resolution and long-wavelength harmonics affect the accuracy of Moho results. After giving a summary of applied methodology (in section 2), we briefly describe input datasets and models (in section 3) and numerical procedures (in section 4). Results are then presented (in section 5) and discussed (in section 6). Finally we summarize major findings (in section 7).

2. Methodology

We applied methods for a spherical harmonic analysis and synthesis of gravitational and crustal structure models to compute the Bouguer gravity data that were subsequently used to estimate the Moho depth based on solving the Vening Meinesz-Moritz (VMM) inverse problem of isostasy [6,12,14]. We also estimated the Moho depth according to the Airy [4] theory. Numerical steps involved in the gravimetric forward and inverse modelling are given next.

2.1. Gravimetric forward modelling

We computed the Bouguer gravity disturbances from the free-air gravity disturbances by applying the topographic and crust-stripping gravity corrections in order to accentuate a gravitational signature of the Moho geometry, while attenuating gravitational signals of the topography and crustal density heterogeneities.

2.1.1. Free-air gravity data

For the external convergence domain $r \geq R$, the free-air gravity disturbance δg^{FA} at a location (r, Ω) is computed from the (fully-normalized) spherical harmonics $T_{n,m}$ of the disturbing potential T (defined as the difference between the actual and normal gravity potentials W and U respectively; $T = W - U$) using the following expression (e.g. [31])

$$\delta g^{\text{FA}}(r, \Omega) = \frac{GM}{R^2} \sum_{n=0}^{\bar{n}} \sum_{m=-n}^n \left(\frac{R}{r}\right)^{n+2} (n+1) T_{n,m} Y_{n,m}(\Omega) \quad (1)$$

where $GM = 3986005 \times 10^8 \text{ m}^3 \text{ s}^{-2}$ is the geocentric gravitational constant, $R = 6371 \times 10^3 \text{ m}$ is the Earth's mean radius, $Y_{n,m}$ are the (fully-normalized) surface spherical functions of degree n and order m , and \bar{n} is the upper summation index of spherical harmonics. The 3D position in Eq. (1) and thereafter is defined in the spherical coordinate system (r, Ω) ; where r is the radius, and $\Omega = (\varphi, \lambda)$ is the spherical direction with the spherical latitude φ and longitude λ .

2.1.2. Bouguer gravity data

As stated above, the Bouguer gravity disturbances δg^{B} were obtained from the free-air gravity disturbances δg^{FA} after applying the topographic and crust-stripping gravity corrections. The application of the topographic gravity correction g^{T} removed the gravitational contribution of topographic masses of a uniform density. Subsequently, the crust-stripping gravity corrections were applied in order to remove gravitational contributions of major known anomalous density structures within the whole crust (down to the Moho interface). Specifically, we applied the gravity corrections due to density contrasts of lakes g^{L} [32], ice g^{I} [33], bathymetry g^{B} and sediments g^{S} . The atmospheric gravity correction was disregarded, having globally maxima less than 1 mGal (cf. [34]). The procedure of computing the Bouguer gravity disturbances is then written as (cf. [19,23])

$$\delta g^{\text{B}} = \delta g^{\text{FA}} - g^{\text{T}} - g^{\text{L}} - g^{\text{I}} - g^{\text{B}} - g^{\text{S}} \quad (2)$$

The topographic gravity correction g^{T} is defined for a uniform topographic density by the following expression

$$g^{\text{T}}(r, \Omega) = \frac{GM}{R^2} \sum_{n=0}^{\bar{n}} \sum_{m=-n}^n \left(\frac{R}{r}\right)^{n+2} (n+1) V_{n,m}^{\text{T}} Y_{n,m}(\Omega) \quad (3)$$

The potential coefficients $V_{n,m}^{\text{T}}$ in Eq. (3) read

$$V_{n,m}^T = \frac{3}{2n+1} \frac{\rho^T}{\bar{\rho}^{\text{Earth}}} \sum_{k=0}^{n+2} \binom{n+2}{k} \frac{(-1)^k}{k+1+i} \frac{H_{n,m}^{(k+1)}}{R^{k+1}} \quad (4)$$

where $\bar{\rho}^{\text{Earth}} = 5500 \text{ kg m}^{-3}$ is the Earth's mean mass density, and ρ^T is the (average) topographic density. The topographic coefficients $\{H_{n,m}^{(k+1)} : k = 0, 1, \dots\}$ are given by

$$H_n^{(k+1)}(\Omega) = \frac{2n+1}{4\pi} \iint_{\Phi} H_U^{k+1}(\Omega') P_n(t) d\Omega' = \sum_{m=-n}^n H_{n,m}^{(k+1)} Y_{n,m}(\Omega) \quad (5)$$

where P_n are the Legendre polynomials for the argument t defined as: $t = (r^2 + r'^2 - \varrho^2)/2rr'$, and ϱ is the Euclidean spatial distance between points (r, Ω) and (r', Ω') . The infinitesimal surface element on the unit sphere is denoted by $d\Omega' = \cos \varphi' d\varphi' d\lambda'$, and Φ is the full spatial angle.

The crust-stripping gravity corrections were computed based on applying the method developed by Tenzer et al. [19] that utilizes the information about a 3D density distribution within a particular geological unit, such as sedimentary basins (see also [20,21,23]).

The generic expression for a spherical harmonic synthesis reads

$$g(r, \Omega) = \frac{GM}{R^2} \sum_{n=0}^{\bar{n}} \sum_{m=-n}^n \left(\frac{R}{r}\right)^{n+2} (n+1) V_{n,m} Y_{n,m}(\Omega) \quad (6)$$

The potential coefficients $V_{n,m}$ of each volumetric mass layer are defined by

$$V_{n,m} = \frac{3}{2n+1} \frac{1}{\bar{\rho}^{\text{Earth}}} \sum_{i=0}^I (F_{n,m}^{(i)} - Fu_{n,m}^{(i)}) \quad (7)$$

where the coefficients $\{F_{n,m}^{(i)}, Fu_{n,m}^{(i)} : i = 0, 1, \dots, I\}$ are defined as follows

$$F_{n,m}^{(i)} = \sum_{k=0}^{n+2} \binom{n+2}{k} \frac{(-1)^k}{k+1+i} \frac{L_{n,m}^{(k+1+i)}}{R^{k+1}}, \quad (8)$$

$$Fu_{n,m}^{(i)} = \sum_{k=0}^{n+2} \binom{n+2}{k} \frac{(-1)^k}{k+1+i} \frac{U_{n,m}^{(k+1+i)}}{R^{k+1}}$$

The coefficients $\{L_{n,m}^{(k+1+i)}, U_{n,m}^{(k+1+i)} : k = 0, 1, \dots ; i = 1, 2, \dots, I\}$ in Eq. (8) describe the geometry and density contrast distribution within a particular volumetric mass layer. These coefficients are generated from discrete data (of depth, thickness and density) using the following expressions for a spherical harmonic analysis [20].

$$L_n^{(k+1+i)}(\Omega) = \begin{cases} \frac{2n+1}{4\pi} \iint_{\Phi} [\rho(D_U, \Omega') - \rho^{\text{ref}}] D_L^{k+1}(\Omega') P_n(t) d\Omega' \\ = \sum_{m=-n}^n L_{n,m}^{(k+1+i)} Y_{n,m}(\Omega) & i=0 \\ \frac{2n+1}{4\pi} \iint_{\Phi} \beta(\Omega') \alpha_i(\Omega') D_L^{k+1+i}(\Omega') P_n(t) d\Omega' \\ = \sum_{m=-n}^n L_{n,m}^{(k+1+i)} Y_{n,m}(\Omega) & i=1, 2, \dots, I \end{cases} \quad (9)$$

and

$$U_n^{(k+1+i)}(\Omega) = \begin{cases} \frac{2n+1}{4\pi} \iint_{\Phi} [\rho(D_U, \Omega') - \rho^{\text{ref}}] D_U^{k+1}(\Omega') P_n(t) d\Omega' \\ = \sum_{m=-n}^n U_{n,m}^{(k+1+i)} Y_{n,m}(\Omega) & i=0 \\ \frac{2n+1}{4\pi} \iint_{\Phi} \beta(\Omega') \alpha_i(\Omega') D_U^{k+1+i}(\Omega') P_n(t) d\Omega' \\ = \sum_{m=-n}^n U_{n,m}^{(k+1+i)} Y_{n,m}(\Omega) & i=1, 2, \dots, I \end{cases} \quad (10)$$

The 3D density contrast with respect to the reference crustal density ρ^{ref} in Eqs. (9) and (10) reads

$$\delta\rho(r, \Omega) = \rho(r, \Omega) - \rho^{\text{ref}} = \rho(D_U, \Omega) - \rho^{\text{ref}} + \beta(\Omega) \sum_{i=1}^I \alpha_i(\Omega) (R-r)^i, \quad \text{for } R - D_U(\Omega) \geq r > R - D_L(\Omega) \quad (11)$$

where $\rho(D_U, \Omega)$ is a (nominal) value of the lateral density at a location Ω and a depth D_U .

2.2. Gravimetric Moho inversion

We applied the Airy and VMM gravimetric methods to estimate the Moho depth. A brief summary of theoretical principles of both methods is given next.

2.2.1. Airy model

According to the Airy local isostatic model, the Moho depth D_M^{Airy} can readily be computed from

$$D_M^{\text{Airy}}(\Omega) = D_0 - \frac{\rho^T H}{\Delta\rho^{c/m}(\Omega)} \quad (12)$$

where ρ^T is the average topographic density, D_0 is the mean depth of the Moho interface, and $\Delta\rho^{c/m}$ denotes a variable density contrast across the Moho interface.

2.2.2. VMM model

Eshagh [15] generalized the VMM inverse problem of isostasy for the variable Moho density contrast. He presented the VMM solution for finding the Moho depth D_M^{VMM} in the following form

$$D_M^{\text{VMM}}(\Omega) = \frac{R}{3} \left[1 - \left(1 - \frac{D_0}{R} \right)^3 \right] \left(1 - \frac{D_0}{R} \right)^{-1} - \frac{1}{4\pi G \Delta\rho^{c/m}(\Omega)} \sum_{n=0}^N \frac{2n+1}{n+1} \delta g_n^B \left(1 - \frac{2+n}{2R} D_0 \right)^{-1} P_n(\sin \phi) \quad (13)$$

where $G = 6.674 \times 10^{-11} \text{ m}^3 \text{ kg}^{-1} \text{ s}^{-2}$ is the Newton's gravitational constant, and δg_n^B are the spherical harmonics of the Bouguer gravity disturbances.

The VMM model in Eq. (13) is suitable for an estimation of the Moho depth only under either the oceanic crust or the continental crust. However, it should not be used for a simultaneous estimation of the Moho depth used the oceanic and continental crust due to large systematic differences between a thick continental crust in

contrast to a much thinner oceanic crust. Eshagh [35] addressed this theoretical deficiency by introducing the degree-dependent Moho parameter β_n in order to account for a generally different average thickness of the oceanic and continental crust. The VMM model in Eq. (13) then becomes [35].

$$D_M^{\text{VMM}}(\Omega) = \frac{R}{3} \left[1 - \left(1 - \frac{D_0}{R} \right)^3 \right] \left(1 - \frac{D_0}{R} \right)^{-1} - \frac{1}{4\pi G \Delta \rho^c / m(\Omega)} \sum_{n=0}^N \frac{2n+1}{n+1} \beta_n \delta g_n^B \left(1 - \frac{2+n}{2R} D_0 \right)^{-1} P_n(\sin \phi) \quad (14)$$

where

$$\beta_n = \begin{cases} \left(1 - (n+2) \frac{D_0}{2R} \right)^{-1} & \text{for continents} \\ 1 & \text{for oceans} \end{cases} \quad (15)$$

The expression given in Eq. (15) was proposed by Eshagh [35] based on testing (global-scale) approximation errors, while checking the Moho-depth degree variances. He realised that beneath the continental crust, the choice of a mean Moho depth D_0 significantly influences Moho depth variations, while causing unrealistic Moho frequencies beneath oceans.

3. Input datasets and models

We used the EIGEN-6C4 [36] global gravitational model, the Earth2014 topographic, bathymetric, inland bathymetry and glacial bedrock relief datasets [37], the marine sediment thickness data [38] and the CRUST1.0 [39] global seismic crustal model. These datasets and models were used for a gravimetric forward modeling of crustal density structures within the study area of the European plate (see Fig. 1). We also used the seismic Moho model of the European plate prepared by Grad et al. [40] to validate our gravimetric results.

The combined gravity field model EIGEN-6C4 was compiled from terrestrial and satellite gravity data including also the satellite gravity-gradiometry data from the Gravity field and steady-state Ocean Circulation Explorer (GOCE; [41,42]) over the entire mission (from November 2009 until October 2013). The combination of different satellite and terrestrial data was done by a band-

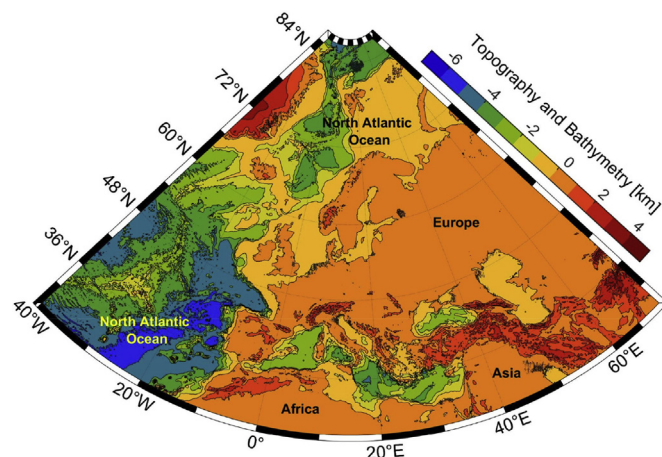


Fig. 1. Topography of the study area.

limited combination of normal equations (to max degree 370), which were generated from observation equations for the spherical harmonic coefficients according to the procedure described by Shako et al. [43]. This solution extended to a maximum degree of 2190 by a block-diagonal solution using the DTU10 global gravity anomaly data grid [44,45].

The Earth2014 datasets [37] provide the information about the topographic heights inland, the bathymetric depths offshore, the glacial bedrock relief in polar regions and the inland bathymetric depths of major lakes on a $1' \times 1'$ grid. This model was compiled from data releases of the SRTM30_PLUSv9 [46], SRTMv4.1 [47], BEDMAP2 [48] and Greenland Bedrock Topography GBTV3 [49].

The dataset of the marine sediment thickness on a $5' \times 5'$ grid was made available through the National Geophysical Data Center (NGDC) of the National Oceanic and Atmospheric Administration (NOAA).

The CRUST1.0 global seismic crustal model was compiled globally on a $1^\circ \times 1^\circ$ grid [39]. It consists of the ice, seawater, (upper, middle, and lower) sediments and (upper, middle, and lower) crystalline crustal layers. It provides also information about a lateral density structure of the upper mantle. Globally averaged data from active seismic methods and deep drilling profiles were used to predict sediment and crustal structures where no seismic measurements were available (most parts of Africa, South America, Greenland, and large oceanic areas) by a generalization to similar geological and tectonic settings.

Grad et al. [40] compiled the first digital, high-resolution Moho depth model (denoted here as EURO) for the whole Europe, extending from the mid-Atlantic ridge in the west to the Ural Mountains in the east, and from the Mediterranean Sea in the south to the Barents Sea and Spitsbergen in the Arctic in the north.

4. Numerical procedures

Expressions for a spherical harmonic analysis and synthesis in section 2 were applied to compute the Bouguer gravity disturbances using input datasets and models summarized in section 3. Numerical procedures applied to compute the Bouguer gravity disturbances and to estimate the Moho depth are briefly reviewed in this section.

4.1. Gravimetric forward modelling

The free-air gravity disturbances and gravity corrections were computed with a spectral resolution complete to the spherical harmonic degree of 2160 (corresponding to a $5' \times 5'$ spatial resolution in terms of a half-wavelength), except for the continental sediment gravity correction. This gravity correction was computed only up to the spherical harmonic degree of 180 that corresponds to a $1^\circ \times 1^\circ$ spatial resolution of the CRUST1.0 model. In this way, the (complete) sediment gravity correction was computed individually for contributions of marine and continental sediments. The former was computed with a $5' \times 5'$ spatial resolution (from the NGDC marine sediment data), and the latter only with a $1^\circ \times 1^\circ$ resolution (from the CRUST1.0 sediment data).

The free-air gravity disturbances were computed from the EIGEN-6C4 gravitational coefficients corrected for the GRS80 [50] normal gravity component. The topographic, lake and ice gravity corrections were computed using the Earth2014 datasets of the topography, inland bathymetry and glacial bedrock relief. The density value of 2670 kg m^{-3} was used to compute the topographic gravity correction. It is worth mentioning that this density value is commonly adopted to represent the continental upper crustal density defined based on the areal proportion of sedimentary and shield rocks (cf. [51]). The freshwater density of 1000 kg m^{-3} was

used to compute the lake gravity correction. The glacial density of 917 kg m^{-3} (cf. [52]) was used to compute the ice gravity correction. We note that the ice density contrast with respect to the value of 2670 kg m^{-3} was used for glacier volumes above the sea level. For the glacier volumes below the sea level we computed the ice density contrast with respect to the value of 2900 kg m^{-3} . We further used the CRUST1.0 sediment data, updated for the sediment layers of the Antarctic continental crust according to Baranov et al. [53], to compute the continental sediment gravity correction. The bathymetric gravity correction was computed using the Earth2014 data of the bathymetric depths. A depth-dependent seawater density model was utilized in the definition of the ocean density contrast. For the reference crustal density of 2900 kg m^{-3} and the surface seawater density of $1027.91 \text{ kg m}^{-3}$ (cf. [54–56]), the nominal ocean density contrast (at zero depth) equals $1872.09 \text{ kg m}^{-3}$. The depth-dependent seawater density model is according to Eq. (11) defined by the following parameters (up to the second-order density term): $\beta = 0.00637 \text{ kg m}^{-3}$, $\alpha_1 = 0.7595 \text{ m}^{-1}$ and $\alpha_2 = -4.3984 \times 10^{-6} \text{ m}^{-2}$ (cf. [57]).

We used the NGDC marine sediment thickness data combined with the density model of marine sediments, developed by Tenzer and Gladkikh [58] based on the analysis of *in situ* density measurements, to compute the marine sediment gravity correction. According to Gu et al. [59], the marine sediment density model ρ^s (in g cm^{-3}) reads

$$\rho^s(T_s, D_w) \cong 1.66 - 5.1 \times 10^{-5} D_w + 0.0037 T_s^{0.766} \quad (16)$$

where D_w denotes the ocean-floor depth (in m), and T_s is the sediment thickness (in m). The value 1.66 g cm^{-3} in Eq. (16) represents the sediment density beneath a thin sedimentary cover (for $T_s \rightarrow 0$) at shallow seafloor depths ($D_w \rightarrow 0$). The second constituent describes the decreasing density with the seafloor depth (reflecting the fact that coarse particles are transported at shorter distances from the coast). The third constituent describes the increasing density with the depth within marine sediment layers (due to the compaction and further lithification); see also Chen et al. [60]. We note that the expression in Eq. (16) was converted into a generalized form given in Eq. (11). Finally, we used the CRUST1.0 data to compute the consolidated crust gravity correction.

All gravity computations were realized on a $5' \times 5'$ spherical grid of surface points within the study area. The gravity corrections are shown in Fig. 2. The intermediate results obtained after applying these gravity corrections to the free-air gravity disturbances are presented in Fig. 3. Statistical summaries of the gravity corrections and the corrected gravity disturbances are given in Tables 1 and 2 respectively.

4.2. Gravimetric Moho recovery

We applied the Airy method (Eq. (12)) to estimate the Moho depth for the uniform and variable Moho density contrast. For the uniform density contrast, we adopted the average value of 485 kg m^{-3} (cf. [22]). For the variable model we computed the Moho density contrast as the difference between the CRUST1.0 upper mantle density values and the reference crustal density of 2900 kg m^{-3} . We used the mean topographic heights down sampled on a $1^\circ \times 1^\circ$ grid from the $1' \times 1'$ Earth2014 topographic data by applying the average operator. For both solutions, the mean value of the Moho depth of 28 km was obtained by averaging the CRUST1.0 Moho depth data over the study area.

It is worth mentioning that different estimates of the average Moho density contrast were reported. Dziewonski and Anderson [61], for instance, adopted the value of 480 kg m^{-3} in the definition of the Preliminary Reference Earth Model (PREM). This value was

derived from the analysis of available global seismic data. Tenzer et al. [19] estimated the average value of the Moho density contrast by minimizing a global spatial correlation between gravity and Moho depth data. They used the Moho information from the CRUST2.0 global seismic crustal model [62]. According to their result, the average value was found to be 520 kg m^{-3} . Later, Tenzer et al. [22] and Tenzer et al. [63] updated this value to 485 and 441 kg m^{-3} , respectively, on the basis of more recent datasets and more accurate numerical models. Sjöberg and Bagherbandi [64] estimated the global average of the Moho density contrast of $448 \pm 187 \text{ kg m}^{-3}$ by solving the VMM problem.

We further estimated the Moho depth according to the VMM models with and without considering the degree-dependent Moho parameter β_n (Eqs. (13) and (14)). Both VMM Moho results were again computed for the uniform and variable Moho density contrast. For the case without considering β_n , we used the mean Moho depth of 37 km selected based on minimizing the RMS of Moho depth differences between the VMM gravimetric and the EURO seismic models. All VMM Moho models were computed with a spectral resolution up to degree of 180. This spectral resolution is often used to compute the gravimetric Moho models. A more detailed analysis and discussion of this numerical aspect is postponed until sections 5 and 6.

5. Results

The Moho depth estimates based on applying the Airy and VMM models are presented and compared with seismic solutions in this section.

5.1. Gravimetric Moho models

The Airy and VMM gravimetric Moho models computed on a $1^\circ \times 1^\circ$ grid within the study area are shown in Fig. 4 and their statistical summary is given Table 3.

5.2. Validation of results

The gravimetric results presented in Fig. 4 were compared with the EURO and CRUST1.0 seismic models. The EURO and CRUST1.0 seismic Moho models are shown in Fig. 5, with their statistical summary in Table 4. The Moho depth differences between the gravimetric and seismic models are plotted in Figs. 6 and 7. Statistics of the Moho depth differences are summarized in Tables 5 and 6.

5.3. Spectral analysis

The VMM Moho results, presented in Fig. 4, were computed with a spectral resolution up to degree of 180. Here we investigated dependence of the Moho results on a spectral resolution of gravity data. The RMS and mean of Moho depth differences between the VMM solutions (for the uniform and variable Moho density contrast) and the EURO seismic model are plotted in Figs. 8 and 9.

To estimate the Moho depth from gravity data, we subtracted the gravitational contribution of the topography and crust density heterogeneities in order to enhance a Moho signature in gravity data. This gravity data, however, still comprises a gravitational signal of deep mantle heterogeneities that should also be modelled and subtracted. Since our knowledge about a deep mantle density structure is limited, this procedure could be realized by subtracting the long-wavelength part of gravity spectrum. It is assumed that low-degree spherical harmonics comprise mainly the gravitational contribution of deep mantle heterogeneities. In Figs. 8 and 9, we inspected this aspect by checking the RMS and mean of the Moho

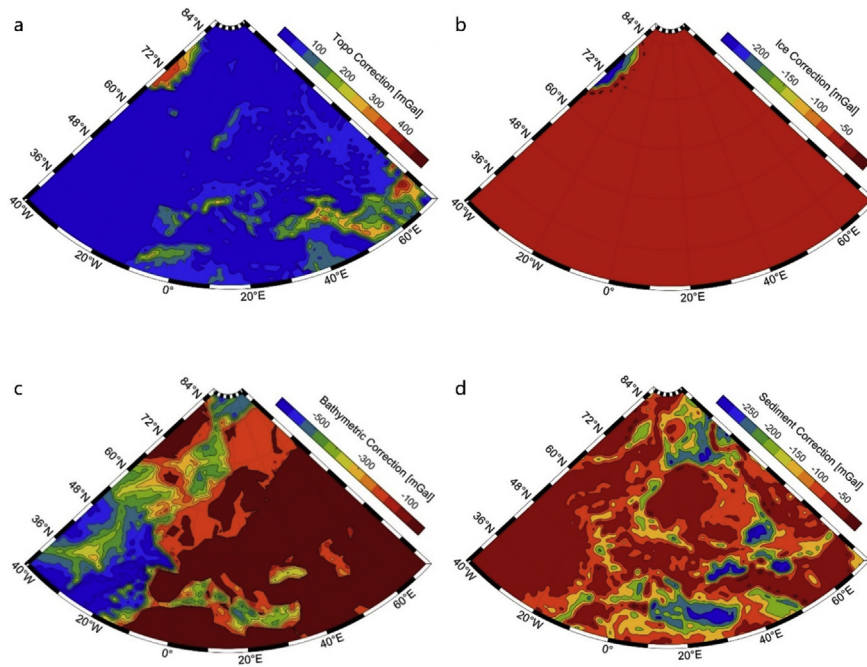


Fig. 2. Gravity corrections: (a) topographic g^T , (b) ice^I g^I , (c) bathymetric g^B , and (d) sediment g^S .

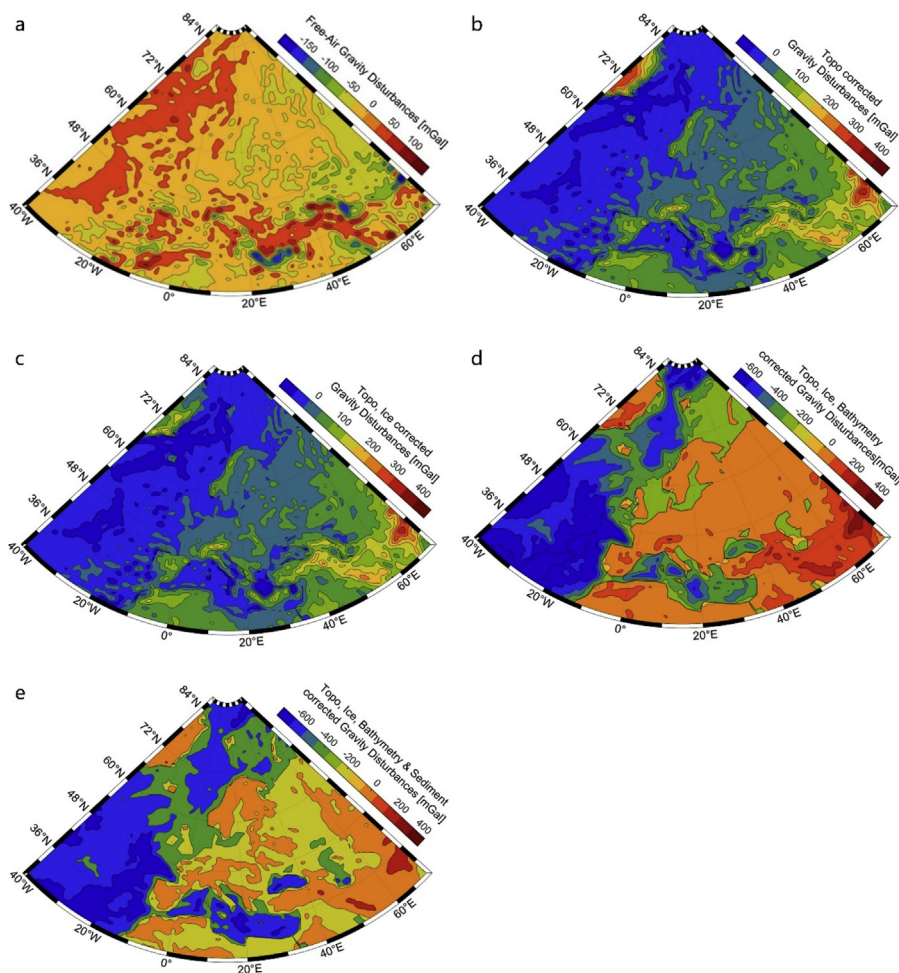


Fig. 3. Regional gravity maps: (a) the free-air gravity disturbances δg^{FA} , (b) the topography-corrected gravity disturbances δg^T , (c) the topography-corrected and lake- and ice-stripped gravity disturbances δg^{TII} , (d) the topography-corrected and lake-, ice- and bathymetry-stripped gravity disturbances δg^{TII^B} , and (e) the (negative) Bouguer gravity disturbances δg^B .

Table 1
Statistics of the gravity corrections. For the notation used, see the legend to Fig. 3.

Gravity Correction	Min [mGal]	Max [mGal]	Mean [mGal]	STD [mGal]
g^T	-2	532	42	72
g^L	-3	20	0	1
g^I	-247	10	-7	26
g^B	-667	0	-182	193
g^S	-333	20	-77	62

Table 2
Statistics of the free-air gravity disturbances and the intermediate results obtained after applying the individual gravity corrections. For the notation used, see the legend to Fig. 2.

Gravity Disturbances	Min [mGal]	Max [mGal]	Mean [mGal]	STD [mGal]
δg^{FA}	-203	158	19	29
δg^T	-117	463	23	73
δg^{TL}	-118	463	23	73
δg^{TLI}	-120	460	15	62
δg^{TLIB}	-659	460	-167	239
δg^B	-765	454	-245	248

Table 3
Statistics of the Airy and VMM gravimetric Moho solutions. For the notation used, see the legend to Fig. 4.

Moho model	Min [km]	Max [km]	Mean [km]	STD [km]
$D_{M,\Delta\rho^c/m}^A$	0.1	56.6	23.3	10.1
$D_{M,\Delta\rho^c/m(\Omega)}^A$	0.3	51.7	24.2	8.1
$D_{M,\Delta\rho^c/m}^{VMM}$	0.9	63.2	26.5	12.6
$D_{M,\Delta\rho^c/m(\Omega)}^{VMM}$	0.9	59.7	28.7	10.1
$D_{M,\Delta\rho^c/m,\beta_n}^{VMM}$	2.7	63.3	26.9	11.5
$D_{M,\Delta\rho^c/m(\Omega),\beta_n}^{VMM}$	4.0	59.8	29.0	9.2

depth differences obtained after removing the long-wavelength contribution for different degrees of spherical harmonics (5, 10, 15 and 20).

6. Discussion of results

The comparison of gravimetric results revealed some substantial discrepancies between the Airy and VMM Moho depth models. Generally, these differences are attributed to adopted compensation mechanism. A local isostatic principle of the Airy theory is

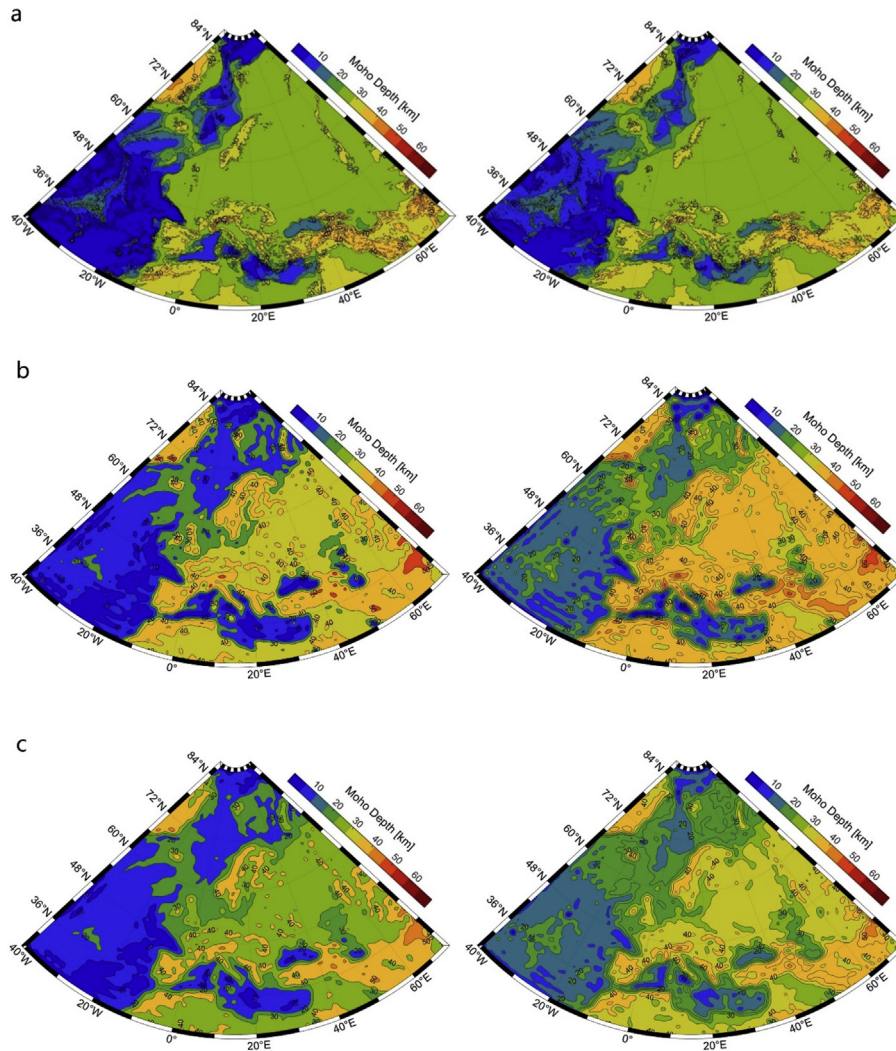


Fig. 4. Gravimetric Moho depth computed by applying: (a) the Airy model for the uniform $D_{M,\Delta\rho^c/m}^A$ (left panel) and variable $D_{M,\Delta\rho^c/m(\Omega)}^A$ (right panel) Moho density contrast, (b) the VMM model for the uniform $D_{M,\Delta\rho^c/m}^{VMM}$ (left panel) and variable $D_{M,\Delta\rho^c/m(\Omega)}^{VMM}$ (right panel) Moho density contrast, and (c) the VMM model with considering the degree-dependent Moho parameter β_n for the uniform $D_{M,\Delta\rho^c/m,\beta_n}^{VMM}$ (left panel) and variable $D_{M,\Delta\rho^c/m(\Omega),\beta_n}^{VMM}$ (right panel) Moho density contrast.

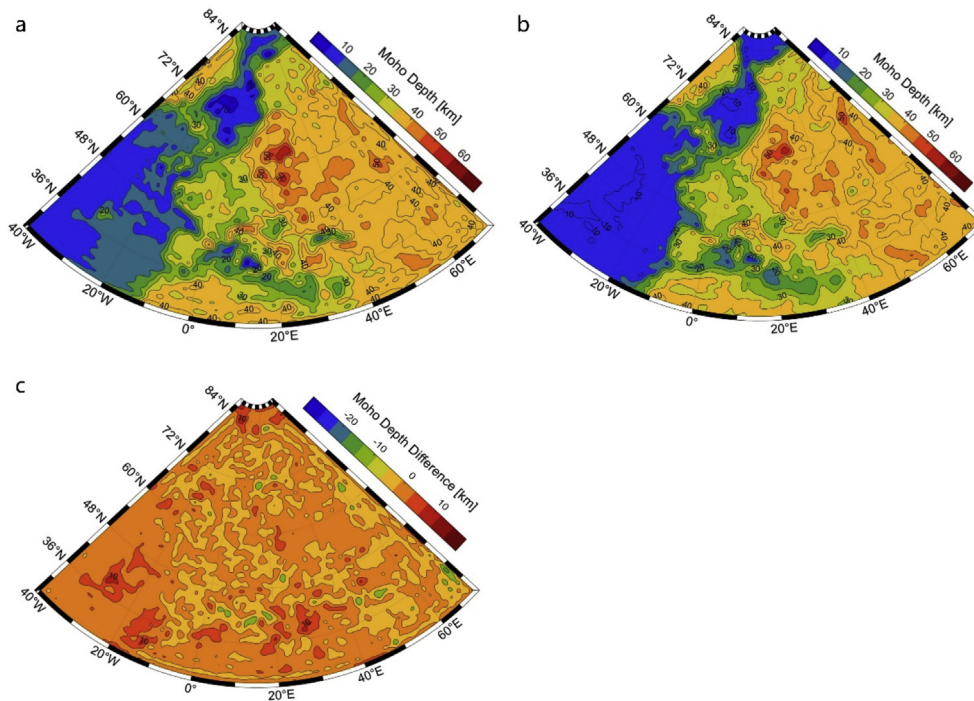


Fig. 5. Seismic Moho models: (a) EURO D_M^{EURO} , (b) CRUST1.0 $D_M^{CRUST1.0}$, and (c) their differences $D_M^{EURO} - D_M^{CRUST1.0}$.

Table 4

Statistics of the EURO and CRUST1.0 seismic Moho models and their differences.

Moho model	Min [km]	Max [km]	Mean [km]	STD [km]
D_M^{EURO}	2.3	59.7	29.7	11.3
$D_M^{CRUST1.0}$	7.1	58.0	28.8	12.0
Moho model differences	Min [km]	Max [km]	Mean [km]	RMS [km]
$D_M^{EURO} - D_M^{CRUST1.0}$	-27.4	14.1	0.8	3.3

exhibited in the Moho geometry (Fig. 4a) by a relatively sharp contrast in crustal thickness across continental margins. Moreover, we could see a quite localized isostatic signature of mountain roots in contrast to a relatively smooth Moho pattern under flat and moderately elevated regions. Differences between the Airy solutions for the uniform and variable Moho density contrast are not significant.

The Moho geometry of all four VMM solutions (Fig. 4b and c) is smoother than the Airy solutions. In this case, however, we could see remarkable differences between VMM solutions computed using the constant and variable Moho density contrast, particularly in their spatial pattern. Differences between the VMM results obtained with and without applying the degree-dependent Moho parameter are much less pronounced. Generally, among all gravimetric results, the VMM models for the variable Moho density contrast most closely agree with seismic models (Fig. 5).

We could identify two dominant features in the VMM Moho results for the variable Moho density contrast. The oldest Archean and Proterozoic crust is characterized by a crustal thickness that typically exceeds 40 km and reaches maxima up to roughly 60 km. The continental Variscan and Alpine crustal structures have a thickness largely between 20 and 40 km. This general classification roughly agrees with the interpretation of seismic data by Grad et al. [40].

A more detailed comparison of gravimetric and seismic models (Fig. 6) confirmed a significantly better agreement of the VMM

solutions with the EURO and CRUST1.0 seismic models. Large systematic discrepancies, on the other hand, exist between the Airy and seismic models that often exceed even 20 km over most of the Russian Platform. The VMM model for the variable Moho density contrast and the degree-dependent Moho parameter has the best agreement (in terms of the RMS and mean of the Moho depth differences) with both seismic models. As seen in Tables 5 and 6, the RMS of differences of this gravimetric solution with both seismic models is roughly 6.5 km, and without the presence of a systematic bias (the mean of differences is less than 1.0 km). According to Knapmeyer-Endrun et al. [65] such differences between gravimetric and seismic solutions are roughly within the limit of tolerance. Nevertheless, we could observe also large regional dissimilarities, particularly over most of the Russian Platform, where the gravimetric model systematically overestimates the Moho depth of about 10 km. Large disagreements there reach locally even 20 km. In the Scandinavian Shield, the Variscan-Alpine orogenic formations and elsewhere, these differences are mostly less than 10 km. Large differences up to about 10–12 km are seen over old parts of the oceanic lithosphere in the eastern Mediterranean Sea. In contrast, the VMM model only slightly underestimates the oceanic crustal thickness in the northeast Atlantic.

The spectral analysis in Figs. 8 and 9 reveals that the best VMM result by means of fitting seismic solutions is attained when using a spectral resolution up to degree of 60. With an increasing spectral resolution, the RMS fit and the systematic bias between the VMM

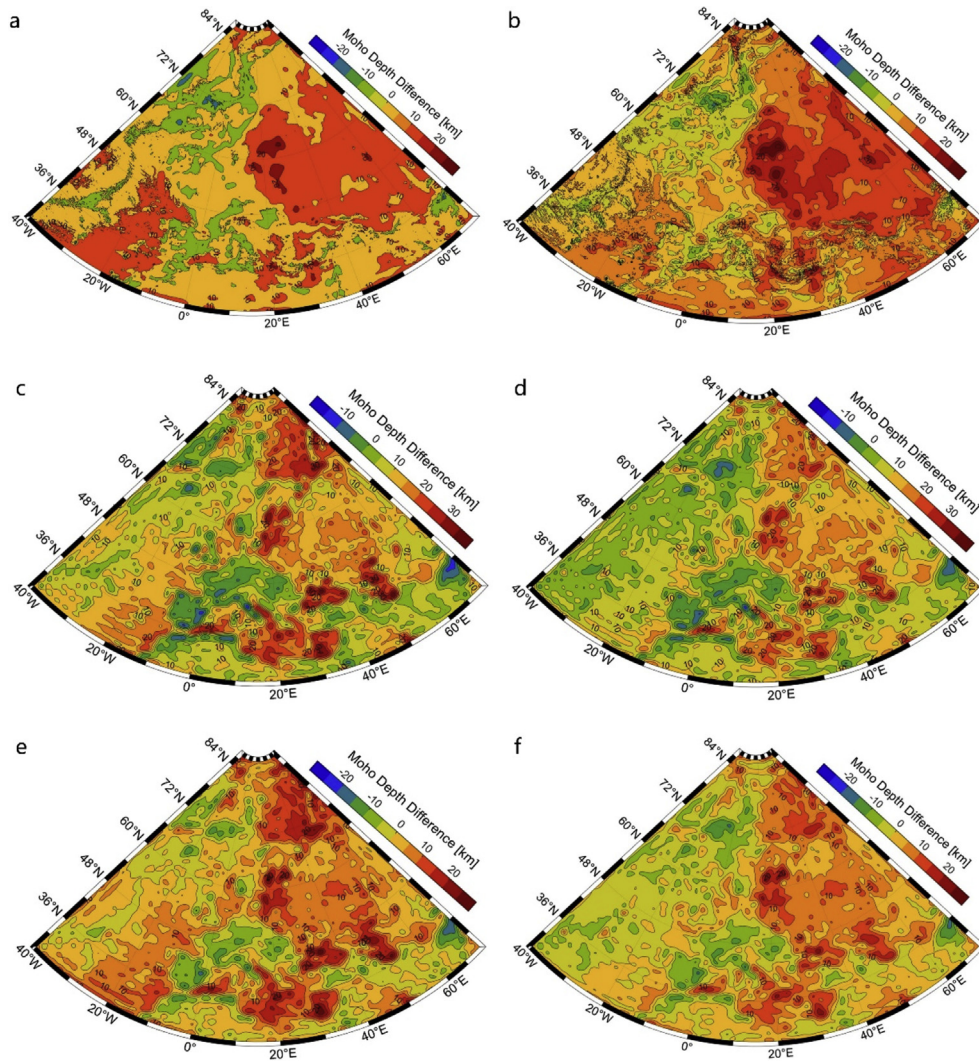


Fig. 6. The Moho depth differences: (a) $D_{M,\Delta\rho^c/m}^A - D_M^{\text{EURO}}$, (b) $D_{M,\Delta\rho^c/m(\Omega)}^A - D_M^{\text{EURO}}$, (c) $D_{M,\Delta\rho^c/m}^{\text{VMM}} - D_M^{\text{EURO}}$, (d) $D_{M,\Delta\rho^c/m(\Omega)}^{\text{VMM}} - D_M^{\text{EURO}}$, (e) $D_{M,\Delta\rho^c/m,\beta_n}^{\text{VMM}} - D_M^{\text{EURO}}$, and (f) $D_{M,\Delta\rho^c/m(\Omega),\beta_n}^{\text{VMM}} - D_M^{\text{EURO}}$. For the notation used, see the legends to Figs. 4 and 5.

and seismic models slightly increase. These changes in the accuracy specifications are, however, in both cases less than 1 km, thus not crucial as an accuracy indicator. Interestingly, however, this finding does not hold for the most optimal scheme for a gravimetric Moho modelling (i.e. the VMM model for the variable Moho density contrast and the degree-dependent Moho parameter). In this case, the systematic bias approaches zero, but the RMS fit of the VMM solution for a spectral resolution up to degree of 60 is slightly worse than for higher spectral resolutions (up to 360). Nevertheless, differences between the RMS fits of VMM models for investigated spectral resolutions (from 60 to 360) are less than 0.5 km. Results of our analysis not presented here in detail, however, revealed that the accuracy could rapidly deteriorate when using a very high degree resolution (>720) to model the Moho geometry.

A rough assessment of the influence of deep mantle gravity heterogeneities on the Moho geometry reveals that modifications in the Moho geometry caused by subtracting the long-wavelength part of gravity spectrum are not significant. The analysis indicates that the best RMS fit and a minimum systematic bias was attained after subtracting low-degree spherical harmonics up to degree of 5 when solving the VMM inverse problem of isostasy for the uniform Moho density contrast and applying the degree-dependent Moho parameter (Fig. 8). Nevertheless, the RMS fit and a systematic bias

between the VMM and seismic models worsen only slightly even after removing low-degree spherical harmonics up to degree 20. We also see that the use of a full harmonic spectrum up to a chosen spectral resolution worsens the RMS fit and a systematic bias to about 0.5 km in both cases when compared with the VMM solution after removing the low-degree harmonics up to degree 5. Similar accuracy characteristics hold also for the VMM solution for the variable Moho density contrast, with the best result obtained after removing spherical harmonics up to degree 5. Interestingly, the VMM solution for a maximum spectral resolution up to degree 60 again behaves differently. The optimal result is obtained after subtracting spherical harmonics up to degree 10, with a minimum systematic bias. Even if the RMS fit worsens after subtracting spherical harmonics above degree 10, the impact on accuracy is stochastically insignificant.

7. Summary and concluding remarks

We have investigated some basic numerical factors and parameters that could affect accuracy characteristics of the Airy and VMM methods for a Moho recovery from gravity data. The accuracy characteristics were assessed with respect to seismic models. In

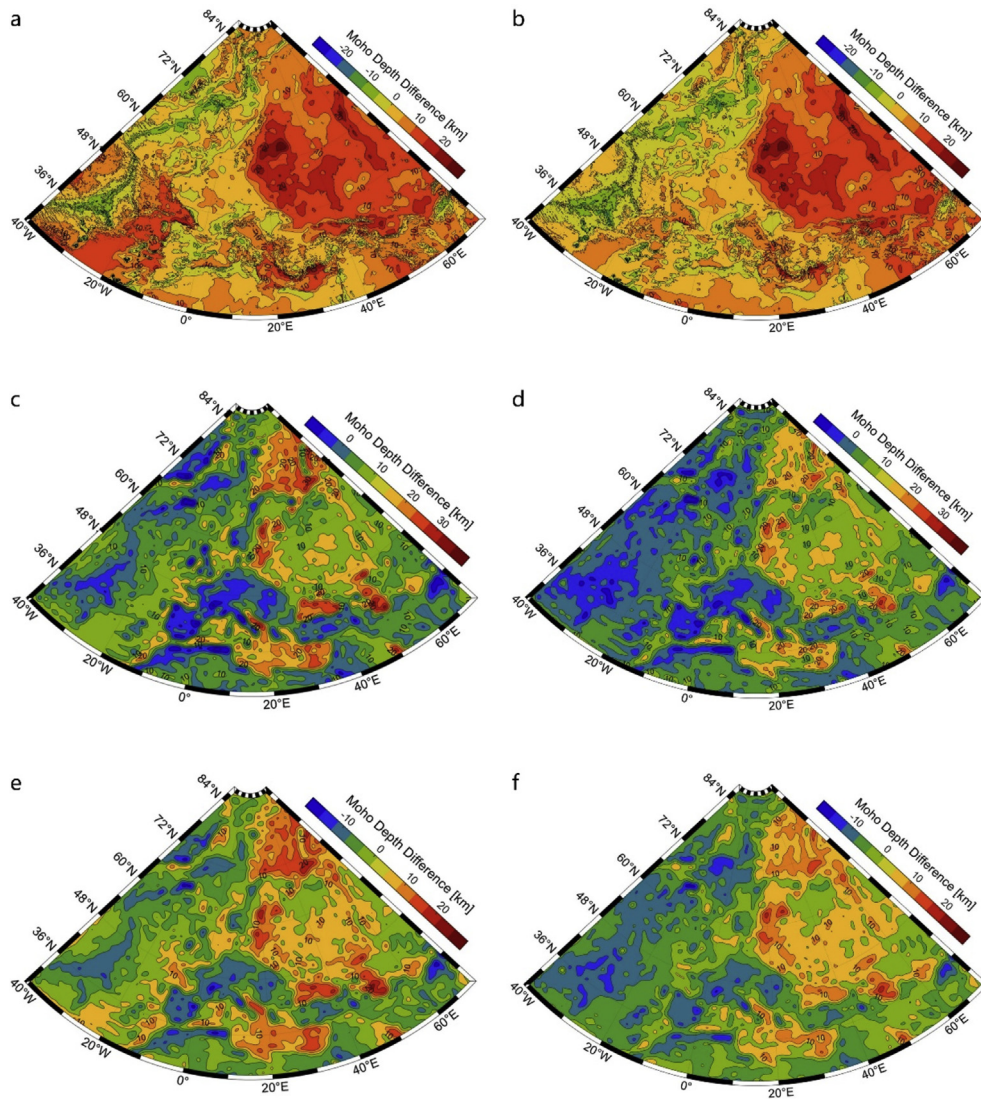


Fig. 7. The Moho depth differences: (a) $D_{M,\Delta\rho^c/m}^A - D_M^{CRUST1.0}$, (b) $D_{M,\Delta\rho^c/m(\Omega)}^A - D_M^{CRUST1.0}$, (c) $D_{M,\Delta\rho^c/m}^{VMM} - D_M^{CRUST1.0}$, (d) $D_{M,\Delta\rho^c/m(\Omega)}^{VMM} - D_M^{CRUST1.0}$, (e) $D_{M,\Delta\rho^c/m,\beta_n}^{VMM} - D_M^{CRUST1.0}$, and (f) $D_{M,\Delta\rho^c/m(\Omega),\beta_n}^{VMM} - D_M^{CRUST1.0}$. For the notation used, see the legends to Figs. 4 and 5.

Table 5

Statistics of the Moho depth differences.

Moho model differences	Min [km]	Max [km]	Mean [km]	RMS [km]
$D_{M,\Delta\rho^c/m}^A - D_M^{EURO}$	-31.1	31.1	6.4	9.3
$D_{M,\Delta\rho^c/m(\Omega)}^A - D_M^{EURO}$	-26.1	31.4	5.5	8.7
$D_{M,\Delta\rho^c/m}^{VMM} - D_M^{EURO}$	-29.6	33.6	3.1	8.5
$D_{M,\Delta\rho^c/m(\Omega)}^{VMM} - D_M^{EURO}$	-29.3	25.0	0.9	7.0
$D_{M,\Delta\rho^c/m,\beta_n}^{VMM} - D_M^{EURO}$	-28.9	27.9	2.7	7.7
$D_{M,\Delta\rho^c/m(\Omega),\beta_n}^{VMM} - D_M^{EURO}$	-29.7	23.3	0.6	6.5

particular, we inspected how the spectral resolution and long-wavelength harmonics affect the Moho results.

According to our findings, the VMM inverse problem of isostasy formulated based on adopting a regional compensation mechanism approximates the seismic Moho geometry much more realistically than the Airy model based on a local compensation mechanism. The application of the variable Moho density contrast improves the VMM gravimetric results. An additional improvement is achieved

by applying the degree-dependent Moho parameter to properly deal with a different thickness of the oceanic and continental crust structures.

The spectral analysis indicates that the choice of a different spectral resolution of gravity data (that does not exceed a maximum degree of 360) for a Moho recovery is not essential. A maximum spectral resolution of gravity data for a Moho recovery could be recommended somewhere between degrees from 60 to

Table 6
Statistics of the Moho depth differences.

Moho model differences	Min [km]	Max [km]	Mean [km]	RMS [km]
$D_{M,\Delta\rho^c/m}^A - D_M^{CRUST1.0}$	-26.4	31.3	6.4	9.3
$D_{M,\Delta\rho^c/m(\Omega)}^A - D_M^{CRUST1.0}$	-22.8	29.6	4.6	8.1
$D_{M,\Delta\rho^c/m}^{VMM} - D_M^{CRUST1.0}$	-13.2	36.4	10.0	12.2
$D_{M,\Delta\rho^c/m(\Omega)}^{VMM} - D_M^{CRUST1.0}$	-13.9	31.5	8.0	10.3
$D_{M,\Delta\rho^c/m,\beta_n}^{VMM} - D_M^{CRUST1.0}$	-19.5	26.2	2.9	7.3
$D_{M,\Delta\rho^c/m(\Omega),\beta_n}^{VMM} - D_M^{CRUST1.0}$	-20.7	22.2	0.8	6.3

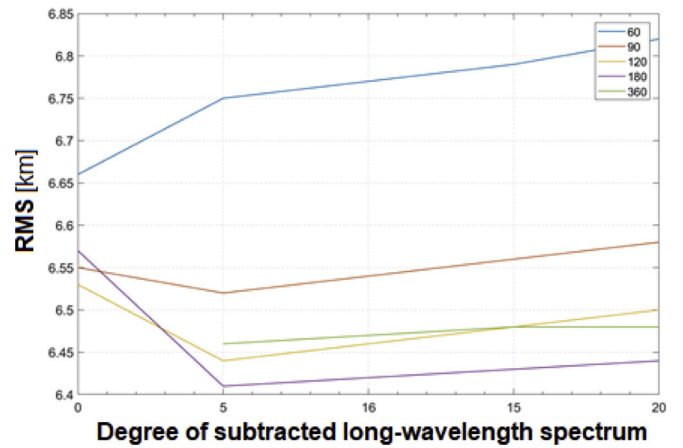
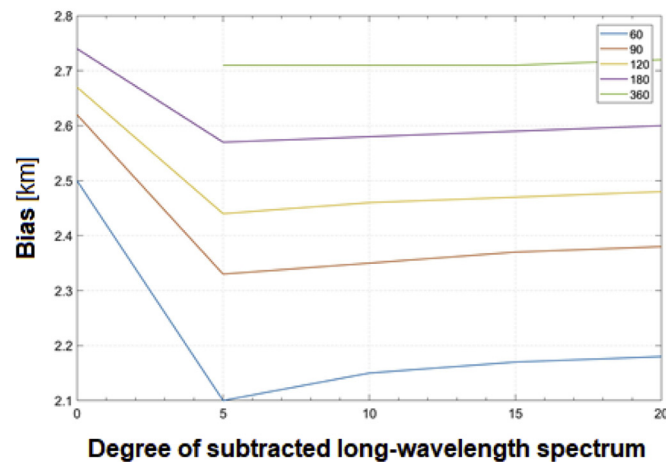
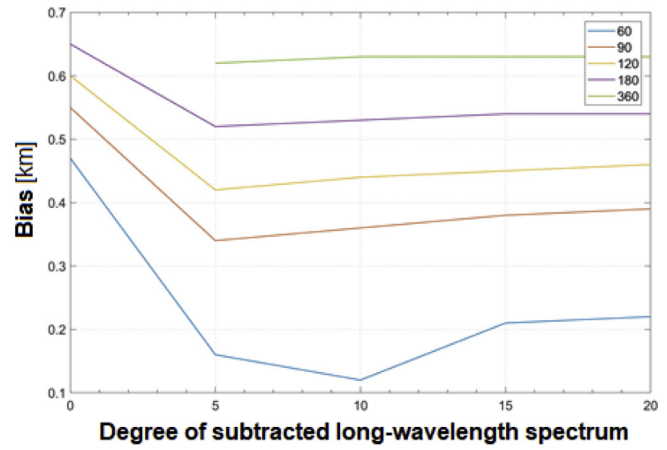
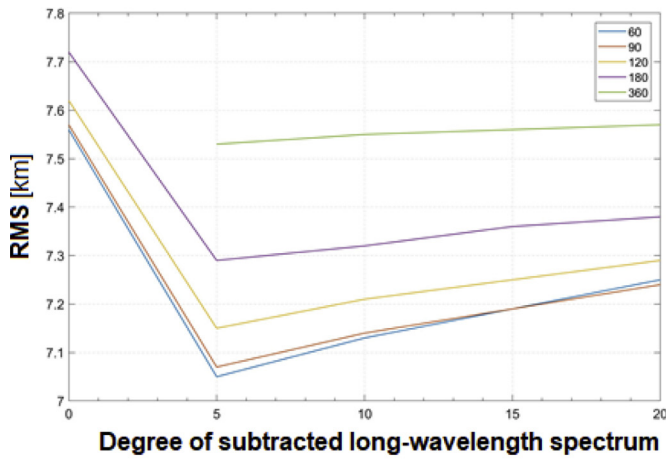


Fig. 8. The RMS and mean of Moho depth differences $D_{M,\Delta\rho^c/m,\beta_n}^{VMM} - D_M^{EURO}$ between the VMM (for the constant Moho density contrast) and EURO models.

Fig. 9. The RMS and mean of Moho depth differences $D_{M,\Delta\rho^c/m(\Omega),\beta_n}^{VMM} - D_M^{EURO}$ between the VMM (for the variable Moho density contrast) and EURO models.

about 180. The use of a very high degree of spherical resolution (above degree 720) could significantly deteriorate the accuracy of a gravimetric Moho modelling.

The spectral analysis also indicates that low-degree spherical harmonics up to degree 5 could be subtracted from the gravity spectrum to solve the VMM inverse problem of isostasy. Nevertheless, the impact of this numerical procedure on the Moho accuracy is stochastically insignificant. This finding, however, holds only for regions with relatively homogenous mantle structure. In global studies as well as studies covering regions characterized by significant mantle density heterogeneities (i.e. subducted slabs, hotspots, mantle upwelling), the long-

wavelength gravity spectrum should be treated more carefully (cf. [28,30]).

Conflict of interest

The authors declare they have no conflict of interest to this work.

Acknowledgments

This research was funded by the Hong Kong Research Grants Council, Project 1-ZE8F: Remote-sensing data for studying Earth's and planetary inner structure.

Appendix A. Supplementary data

Supplementary data to this article can be found online at <https://doi.org/10.1016/j.jgeog.2019.05.003>.

References

- [1] J.H. Pratt, On the attraction of the Himalaya Mountains, and of the elevated regions beyond them, upon the plumb-line in India, *Phil. Trans. Roy. Soc. Lond.* 145 (1855) 53–100.
- [2] J.F. Hayford, *Geodesy: The Figure of the Earth and Isostasy from Measurements in the United States (No 82)*, US Government Printing Office, 1909.
- [3] J. Hayford, W. Bowie, *Geodesy: Effect of Topography and Isostatic Compensation upon the Intensity of Gravity Special Publication No. 10*, U.S. Coast and Geodetic Survey, 1912.
- [4] G.B. Airy, On the computation of the effect of the attraction of mountain-masses, as disturbing the apparent astronomical latitude of stations in geodetic surveys, *Phil. Trans. Roy. Soc. Lond.* 145 (1855) 101–104.
- [5] W.A. Heiskanen, F.A. Vening Meinesz, *The Earth and its Gravity Field*, McGraw-Hill Book Company, Inc, 1958.
- [6] F.A. Vening Meinesz, Une nouvelle méthode pour la réduction isostatique régionale de l'intensité de la pesanteur, *Bull. Geod.* 29 (1931) 33–51.
- [7] R.L. Parker, The rapid calculation of potential anomalies, *Geophys. J. R. Astron. Soc.* 31 (1972) 447–455.
- [8] D.W. Oldenburg, The inversion and interpretation of gravity anomalies, *Geophysics* 39 (4) (1974) 526–536.
- [9] D. Gomez-Ortiz, B.N.P. Agarwal, 3DINVER.M: a MATLAB program to invert the gravity anomaly over a 3D horizontal density interface by Parker Oldenburg's algorithm, *Geoscience* 31 (2005) 513–520.
- [10] Y.H. Shin, H. Xu, C. Braitenberg, J. Fang, Y. Wang, Moho undulations beneath Tibet from GRACE integrated gravity data, *Geophys. J. Int.* 170 (2007) 971–985.
- [11] R. Kiamehr, D. Gomes-Ortiz, A New 3D Moho Depth Model for IRAN Based on the Terrestrial Gravity Data and EGM2008 Model. EGU General Assembly vol. 11, 2009. EGU2009-E2321-1, Vienna, Austria (Abstract).
- [12] H. Moritz, *The Figure of the Earth*, Wichmann, H, Karlsruhe, 1990.
- [13] L.M. Dorman, *The Theory of the Determination of the Earth's Isostatic Response to a Concentrated Load*, University of Wisconsin-Madison, 1970.
- [14] L.E. Sjöberg, Solving vening Meinesz–Moritz inverse problem in isostasy, *Geophys. J. Int.* 179 (3) (2009) 1527–1536.
- [15] M. Eshagh, M. Hussain, R. Tenzer, M. Romeshkani, Moho density contrast in central Eurasia from GOCE gravity gradients, *Rem. Sens.* 8 (418) (2016) 1–18.
- [16] Z. Ye, R. Tenzer, L. Liu, Comparison of spectral and spatial methods for a Moho recovery from gravity and vertical gravity-gradient data, *Studia Geophys. Geod.* 61 (3) (2017) 469–496.
- [17] K. Chakraborty, B. Agarwal, Mapping of crustal discontinuities by wavelength filtering of the gravity FIELD1, *Geophys. Prospect.* 40 (7) (1992) 801–822.
- [18] J.P. Lefort, B.N.P. Agarwal, Gravity and geomorphological evidence for a large crustal bulge cutting across Brittany (France): a tectonic response to the closure of the Bay of Biscay, *Tectonophysics* 323 (3) (2000) 149–162.
- [19] R. Tenzer, Hamayun, P. Vajda, Global maps of the CRUST2.0 components stripped gravity disturbances, *J. Geophys. Res.* 114 (2009a) B05408.
- [20] R. Tenzer, P. Novák, P. Vajda, V. Gladkikh, Hamayun, Spherical harmonic analysis and synthesis of Earth's crust gravity field, *Comput. Geosci.* 16 (1) (2012a) 193–207.
- [21] R. Tenzer, V. Gladkikh, P. Vajda, P. Novák, Spatial and spectral analysis of refined gravity data for modelling the crust-mantle interface and mantle-lithosphere structure, *Surv. Geophys.* 33 (5) (2012b) 817–839.
- [22] R. Tenzer, Hamayun, P. Novák, V. Gladkikh, P. Vajda, Global crust-mantle density contrast estimated from EGM2008, DTM2008, CRUST2.0, and ICE-5G, *Pure Appl. Geophys.* 169 (9) (2012e) 1663–1678.
- [23] R. Tenzer, W. Chen, D. Tsoulis, M. Bagherbandi, L.E. Sjöberg, P. Novák, S. Jin, Analysis of the refined CRUST1.0 crustal model and its gravity field, *Surv. Geophys.* 36 (1) (2015a) 139–165.
- [24] R. Tenzer, W. Chen, S. Jin, Effect of the upper mantle density structure on the Moho geometry, *Pure Appl. Geophys.* 172 (6) (2015b) 1563–1583.
- [25] Y. Jin, M.K. McNutt, Y. Zhu, Evidence from gravity and topography data for folding of Tibet, *Nature* 371 (6499) (1994) 669–674.
- [26] Y.H. Shin, K.S. Choi, H. Xu, Three-dimensional forward and inverse models for gravity fields based on the Fast Fourier Transform, *Comput. Geosci.* 32 (6) (2006) 727–738.
- [27] D. Gómez-Ortiz, B.N.P. Agarwal, R. Tejero, J. Ruiz, Crustal structure from gravity signatures in the Iberian Peninsula, *Geol. Soc. Am. Bull.* 123 (7–8) (2011) 1247–1257.
- [28] M. Bagherbandi, L.E. Sjöberg, Non-isostatic effects on crustal thickness: a study using CRUST2.0 in Fennoscandia, *Phys. Earth Planet In.* 200–201 (2012) 37–44.
- [29] D.H. Eckhardt, The gains of small circular, square and rectangular filters for surface waves on a sphere, *Bull. Geod.* 57 (1983) 394–409.
- [30] M. Bagherbandi, R. Tenzer, L.E. Sjöberg, P. Novák, Improved global crustal thickness modeling based on the VMM isostatic model and non-isostatic gravity correction, *J. Geodyn.* 66 (2013) 25–37.
- [31] W.H. Heiskanen, H. Moritz, *Physical Geodesy*, Freeman WH and Co, San Francisco, 1967.
- [32] R. Tenzer, I. Foroughi, M. Pitoňák, M. Šprlák, Effect of the Earth's inner structure on the gravity in definitions of height systems, *Geophys. J. Int.* 209 (1) (2017) 297–316.
- [33] R. Tenzer, A. Abdalla, P. Vajda, Hamayun, The spherical harmonic representation of the gravitational field quantities generated by the ice density contrast, *Contrib. Geophys. Geodes.* 40 (3) (2010a) 207–223.
- [34] R. Tenzer, P. Vajda, Hamayun, Global atmospheric corrections to the gravity field quantities, *Contrib. Geophys. Geodes.* 39 (3) (2009b) 221–236.
- [35] M. Eshagh, On the approximations in formulation of the Vening Meinesz–Moritz inverse problem of isostasy, *Geophys. J. Int.* 210 (2017) 500–508.
- [36] C. Förste, S.L. Bruinsma, O. Abrikosov, J.M. Lemoine, J.C. Marty, F. Flechtner, G. Balmino, F. Barthelmes, R. Biancale, EIGEN-6C4 the Latest Combined Global Gravity Field Model Including GOCE Data up to Degree and Order 2190 of GFZ Potsdam and GRGS Toulouse. GFZ Data Services Tapley BD, Bettadpur S, Watkins M, 2014.
- [37] C. Hirt, M. Rexer, Earth2014: 1 arc-min shape, topography, bedrock and ice-sheet models - available as gridded data and degree-10,800 spherical harmonics, *Int. J. Appl. Earth Obs. Geoinf.* 39 (2015) 103–112.
- [38] D.L. Divins, *Total Sediment Thickness of the World's Oceans and Marginal Seas*, NOAA Natl Geophys Data Cent, Boulder, Colorado, 2003.
- [39] G. Laske, G. Masters, Z. Ma, M.E. Pasyanos, Update on CRUST1.0 - a 1-degree global model of Earth's crust, *Geophys. Res. Abstr.* 15 (2013) 2658.
- [40] M. Grad, T. Tiira, ESC Working Group, The Moho depth map of the European plate, *Geophys. J. Int.* 176 (2009) 279–292.
- [41] M.R. Drinkwater, R. Floberghagen, R. Haagmans, D. Muzi, A. Popescu, GOCE: ESA's first Earth Explorer Core mission, in: G. Beutler, et al. (Eds.), *Earth Gravity Field from Space-From Sensors to Earth Science*, Space Sci Ser 18, Kluwer Acad, Dordrecht, Netherlands, 2003, pp. 419–432. ISSI.
- [42] R. Floberghagen, M. Fehringer, D. Lamarre, D. Muzi, B. Frommknecht, C. Steiger, J. Piñeiro, A. da Costa, Mission design, operation and exploitation of the gravity field and steady-state ocean circulation explorer mission, *J. Geod.* 85 (11) (2011) 749–758.
- [43] R. Shako, C. Förste, O. Abrikosov, S. Bruinsma, J.-C. Marty, J.M. Lemoine, C. Dahle, EIGEN-6C: a high-resolution global gravity combination model including GOCE data, in: *Observation of the System Earth from Space - CHAMP, GRACE, GOCE and Future Missions*, 2013, pp. 155–161.
- [44] O.B. Andersen, P. Knudsen, P. Berry, The DNSCO8GRA global marine gravity field from double retracked satellite altimetry, *J. Geod.* 84 (3) (2010) 191–199.
- [45] O.B. Andersen, The DTU10 Gravity Field and Mean Sea Surface, in: *Second International Symposium of the Gravity Field of the Earth (IGFS2)*, Fairbanks, Alaska, 2010.
- [46] J.J. Becker, D.T. Sandwell, W.H.F. Smith, J. Braud, B. Binder, J. Depner, D. Fabre, J. Factor, S. Ingalls, S.-H. Kim, R. Ladner, K. Marks, S. Nelson, A. Pharaoh, R. Trimmer, J. Von Rosenberg, G. Wallace, P. Weatherall, Global bathymetry and elevation data at 30 arc seconds resolution: SRTM30_PLUS, *Mar. Geod.* 32 (4) (2009) 355–371.
- [47] A. Jarvis, H.I. Reuter, A. Nelson, E. Guevara, Hole-filled SRTM for the Globe Version 4, Available from the CGIAR-SX1 SRTM 90m Database, 2008 available at: <http://srtm.csi.cgiar.org>.
- [48] P. Fretwell, H.D. Pritchard, D.G. Vaughan, J.L. Bamber, N.E. Barrand, R. Bell, C. Bianchi, R.G. Bingham, D.D. Blankenship, G. Casassa, G. Catania, D. Callens, H. Conway, A.J. Cook, H.F.J. Corr, D. Damaske, V. Damm, F. Ferraccioli, R. Forsberg, S. Fujita, Y. Gim, P. Gogineni, J.A. Griggs, R.C.A. Hindmarsh, P. Holmlund, J.W. Holt, R.W. Jacobel, A. Jenkins, W. Jokat, T. Jordan, E.C. King, J. Kohler, W. Krabill, M. Riger-Kusk, K.A. Langley, G. Leitchenkov, C. Leuschen, B.P. Luyendyk, K. Matsuoka, J. Mouginot, F.O. Nitsche, Y. Nogi, O.A. Nost, S.V. Popov, E. Rignot, D.M. Rippin, A. Rivera, J. Roberts, N. Ross, M.J. Siegert, A.M. Smith, D. Steinhage, M. Studinger, B. Sun, B.K. Tinto, B.C. Welch, D. Wilson, D.A. Young, C. Xiangbin, A. Zirizzotti, Bedmap2: improved ice bed, surface and thickness datasets for Antarctica, *Cryosphere* 7 (2013) 375–393.
- [49] J.L. Bamber, J.A. Griggs, R.T.W.L. Hurkmans, J.A. Dowdeswell, S.P. Gogineni, I. Howat, J. Mouginot, J. Paden, S. Palmer, E. Rignot, D. Steinhage, A new bed elevation dataset for Greenland, *Cryosphere* 7 (2013) 499–510.
- [50] H. Moritz, Geodetic reference system 1980, *J. Geod.* 74 (2000) 128162.
- [51] W.J. Hinze, Bouguer reduction density, why 2.67? *Geophysics* 68 (5) (2003) 1559–1560.
- [52] J.D. Cutnell, W.J. Kenneth, *Physics*, third ed., Wiley, New York, 1995.
- [53] A. Baranov, R. Tenzer, M. Bagherbandi, Combined gravimetric-seismic crustal model for Antarctica, *Surv. Geophys.* 39 (1) (2018) 23–56.
- [54] V. Gladkikh, R. Tenzer, A mathematical model of the global ocean saltwater density distribution, *Pure Appl. Geophys.* 169 (1–2) (2011) 249–257.
- [55] R. Tenzer, P. Vajda, Hamayun, A mathematical model of the bathymetry-generated external gravitational field, *Contrib. Geophys. Geodes.* 40 (1) (2010b) 31–44.
- [56] R. Tenzer, P. Novák, V. Gladkikh, On the accuracy of the bathymetry-generated gravitational field quantities for a depth-dependent seawater density distribution, *Studia Geophys. Geod.* 55 (4) (2011) 609–626.
- [57] R. Tenzer, P. Novák, V. Gladkikh, The bathymetric stripping corrections to gravity field quantities for a depth-dependent model of the seawater density, *Mar. Geod.* 35 (2012c) 198–220.
- [58] R. Tenzer, V. Gladkikh, Assessment of density variations of marine sediments with ocean and sediment depths, *Sci. World J.* 823296 (2014) 9.
- [59] X. Gu, R. Tenzer, V. Gladkikh, Empirical models of the ocean-sediment and marine sediment-bedrock density contrasts, *Geosci. J.* 18 (4) (2014) 439–447.
- [60] W. Chen, R. Tenzer, X. Gu, Sediment stripping correction to marine gravity data, *Mar. Geod.* 37 (4) (2014) 419–439.

- [61] A.M. Dziewonski, D.L. Anderson, Preliminary reference Earth model, *Phys. Earth Planet. In.* 25 (1981) 297–356.
- [62] C. Bassin, G. Laske, T.G. Masters, The current limits of resolution for surface wave tomography in North America, *EOS Trans. AGU* 81 (2000) F897.
- [63] R. Tenzer, M. Bagherbandi, P. Vajda, Global model of the upper mantle lateral density structure based on combining seismic and isostatic models, *Geosci. J.* 17 (1) (2013a) 65–73.
- [64] L.E. Sjöberg, M. Bagherbandi, A method of estimating the Moho density contrast with a tentative application by EGM08 and CRUST2.0, *Acta Geophys.* 58 (2011) 1–24.
- [65] B. Knapmeyer-Endrun, F. Krüger, Group TPW, Moho depth across the trans-European suture zone from P- and S-receiver functions, *Geophys. J. Int.* 197 (2) (2014) 1048–1075.



MSc. Samurdhika Rathnayake. Samurdhika Rathnayake is a PhD candidate in the Department of Land Surveying and Geo-Informatics at the Hong Kong Polytechnic University. She received her B.Sc degree (2016) at the Sabaragamuwa University in Sri Lanka. Her research interest is related to gravimetric modelling of Earth's inner structure.



Assist. Prof. Ing. Robert Tenzer, PhD, Ph.D. Dr. Tenzer is the assistant professor in the Department of Land Surveying and Geo-Informatics at the Hong Kong Polytechnic University. He received MSc in Geodesy and Cartography (in 1995) and PhD in Physical Geodesy (in 1999) at the Slovak Technical University, as well as PhD in Satellite Geodesy (in 2008) at the Czech Technical University. Between 2001 and 2008, he held research positions at the University of New Brunswick, the University of Newcastle upon Tyne and the Delft University of Technology. Between 2009 and 2012, he taught at the University of Otago. Between 2012 and 2016, he was a visiting professor in the School of Geodesy and Geomatics at the Wuhan University. His research interests cover broad areas of Geodesy, Geophysics, Geodynamic and Planetary Science, with a major focus on geospatial modeling techniques and interpretations, theoretical geodesy and geophysics, geo-referencing, planetary inner structure and processes. He is the author of 4 books and more than 200 research journal articles (157 records on Scopus, 129 records on WoS). He presented his research in 195 conference contributions and 60 invited lectures at universities around the world. He is the member of editorial board and scientific adviser to several journals, while also contributing as the reviewer to more than 40 journals (including *Nature Geoscience*). Currently, he is the chair of the International Association of Geodesy (IAG) study group IC-SG7: Earth's inner structure from combined geophysical sources.